Ultrasonics 56 (2015) 399–408

Contents lists available at ScienceDirect

Ultrasonics

journal homepage: www.elsevier.com/locate/ultras

Ultrasound speckle tracking for radial, longitudinal and circumferential strain estimation of the carotid artery – An *in vitro* validation via sonomicrometry using clinical and high-frequency ultrasound

Matilda Larsson [a,b,*], Brecht Heyde [b], Florence Kremer [b], Lars-Åke Brodin [a], Jan D'hooge [b]

[a] Department of Medical Engineering, School of Technology and Health, KTH Royal Institute of Technology, Stockholm, Alfred Nobels Allé 10, 141 52 Huddinge, Sweden
[b] Lab on Cardiovascular Imaging & Dynamics, KU Leuven, Campus Gasthuisberg O&N1, Herestraat 49 box 911, 3000 Leuven, Belgium

ARTICLE INFO

Article history:
Received 11 May 2014
Received in revised form 14 August 2014
Accepted 9 September 2014
Available online 18 September 2014

Keywords:
Ultrasound speckle tracking
Carotid strain
Vessel phantom
High-frequency ultrasound
Sonomicrometry

ABSTRACT

Ultrasound speckle tracking for carotid strain assessment has in the past decade gained interest in studies of arterial stiffness and cardiovascular diseases. The aim of this study was to validate and directly contrast carotid strain assessment by speckle tracking applied on clinical and high-frequency ultrasound images *in vitro*. Four polyvinyl alcohol phantoms mimicking the carotid artery were constructed with different mechanical properties and connected to a pump generating carotid flow profiles. Gray-scale ultrasound long- and short-axis images of the phantoms were obtained using a standard clinical ultrasound system, Vivid 7 (GE Healthcare, Horten, Norway) and a high-frequency ultrasound system, Vevo 2100 (FUJIFILM, VisualSonics, Toronto, Canada) with linear-array transducers (12L / MS250). Radial, longitudinal and circumferential strains were estimated using an in-house speckle tracking algorithm and compared with reference strain acquired by sonomicrometry. Overall, the estimated strain corresponded well with the reference strain. The correlation between estimated peak strain in clinical ultrasound images and reference strain was 0.91 ($p < 0.001$) for radial strain, 0.73 ($p < 0.001$) for longitudinal strain and 0.90 ($p < 0.001$) for circumferential strain and for high-frequency ultrasound images 0.95 ($p < 0.001$) for radial strain, 0.93 ($p < 0.001$) for longitudinal strain and 0.90 ($p < 0.001$) for circumferential strain. A significant larger bias and root mean square error was found for circumferential strain estimation on clinical ultrasound images compared to high frequency ultrasound images, but no significant difference in bias and root mean square error was found for radial and longitudinal strain when comparing estimation on clinical and high-frequency ultrasound images. The agreement between sonomicrometry and speckle tracking demonstrates that carotid strain assessment by ultrasound speckle tracking is feasible.

1. Introduction

Methods for early detection and risk stratification in cardiovascular diseases are of major importance for the prevention of acute ischemic events such as stroke and myocardial infarction. Arterial stiffness describes the rigidity of the arterial wall. An increase in arterial stiffness is one of the most important risk factors of cardiovascular mortality [1]. Since changes in arterial stiffness are thought to occur before clinically apparent cardiovascular disease, methods for arterial stiffness assessment are essential in order to detect, predict and prevent cardiovascular diseases. Moreover, risk stratification is needed in patients with an already established atherosclerotic disease, to provide appropriate interventional treatment strategies and prevent plaque rupture, which is a common cause of acute ischemic events [2].

Ultrasound-based methods are commonly used to assess mechanical properties of arterial walls in studies of arterial stiffness and atherosclerosis. As such, intima-media thickening is considered as a marker of atherosclerosis [3], whereas pulse wave velocity [1,4], arterial distensibility [5,6] and β-stiffness index [7] are common measures of arterial stiffness that have been associated with cardiovascular risk. Recently, novel methods based on shear wave propagation have been developed to assess elastic properties of the artery [8]. Still, there is need for a standardized method assessing arterial stiffness in a reproducible manner.

Historically, ultrasound imaging has been used to confirm plaque presence and estimate the extent of the flow limiting stenosis [9], although more recent studies have shown that plaque rupture

* Corresponding author at: School of Technology and Health, KTH, Alfred Nobels Allé 10, SE-141 52 Huddinge, Sweden. Tel.: + 46 8 790 48 23; fax: + 46 8 21 83 68.
E-mail address: matilda.larsson@sth.kth.se (M. Larsson).

http://dx.doi.org/10.1016/j.ultras.2014.09.005
0041-624X/

and thrombosis, rather than the stenosis, precipitate most acute ischemic events [2]. Typically, vulnerable plaques at high risk of rupture and thrombosis are characterized by active inflammation, large lipid core, thin fibrous cap, intraplaque hemorrhage, and neovascularization of the vasa vasorum [2,10–12]. Accordingly, assessment of properties correlated with plaque composition is needed for plaque characterization and risk stratification. Today, common ultrasound-based methods for this purpose in clinical practice are mainly limited to visual assessment and evaluation of plaque morphology and echolucency [13,14].

Ultrasound speckle tracking is a technique that allows for assessment of tissue motion and deformation by tracking interference patterns across imaging frames. The technique has to a large extent been developed and applied for assessment of mechanical properties of the myocardium [15], whereas speckle tracking-based arterial strain assessment has gained interest in recent years [16–18]. Speckle tracking and tissue Doppler imaging techniques have shown potential in both subclinical detection of increased arterial stiffness, as lower arterial strain values were associated with increased cardiovascular risk [19,20], and in the assessment of plaque characteristics to predict plaque rupture, as strain correlated with plaque composition [21,22].

Assessing strain in the arterial wall and in atherosclerotic plaques is particularly challenging because of the small structures involved and their low physiologic deformation in relation to the applied ultrasound wavelength used in clinical ultrasound systems. A variety of methods enabling measurements of radial and circumferential arterial strain have been developed and applied both in phantom setups and *in vivo* [5,17,18,20,23–25]. During the last decade, methods to assess motion and strain in the longitudinal axis of the arterial wall have also been presented [26–29]. The longitudinal motion of the artery has been neglected and is difficult to assess due to the low amplitudes combined with the intrinsic lower spatial resolution in the azimuth direction. However, with improved imaging techniques it has been demonstrated that the longitudinal motion of the arterial wall during systole can be measured using ultrasound speckle tracking [26,30].

We recently developed a speckle tracking algorithm with parameters tuned for the vascular setting to be used in the characterization of arterial wall mechanics by estimating the in-plane wall strain tensor [27]. The feasibility of the algorithm to assess radial and longitudinal strain of the carotid artery using standard clinical equipment based on simulated data sets was already shown [27]. Moreover, preliminary results from strain assessment *in vitro* using clinical ultrasound in a set of three phantoms have been demonstrated [31]. Despite promising results when using standard clinical ultrasound, the *in vivo* setting most likely requires a higher spatial resolution and improved tracking quality compared to the *in silico* setting, in particular for motion estimation in the lateral dimension with an intrinsically lower spatial resolution than the axial dimension.

The development of high-frequency ultrasound systems has allowed non-invasive micro-imaging for small animal research purposes. High-frequency ultrasonography increases the spatial resolution of images dramatically and it has been applied in e.g. strain measurements in the murine aorta [32]. The use of high-frequency ultrasound in humans is limited due to the low penetration depth. However, the technique has been applied in human vascular research for imaging of vessels for thickness measurements of the three layers of the carotid artery, which has been suggested as a more reliable measure of cardiovascular risk rather than intima-media thickness [33].

Although different speckle tracking algorithms have shown promising results in arterial strain imaging *in silico* and *in vitro*, a thorough experimental validation of the full strain tensor of the carotid artery wall via an independent method is lacking. Moreover, high-frequency ultrasound may improve arterial speckle tracking performance because of the higher-quality images with increased spatial resolution. Consequently, the aim of the present study was to validate and directly contrast radial, longitudinal and circumferential strain assessment by speckle tracking applied on standard clinical and high-frequency ultrasound gray-scale images of gel phantoms mimicking the carotid artery.

2. Methods

A dynamic setup consisting of a carotid artery gel phantom connected to a programmable pulsatile flow pump was built to validate the speckle tracking algorithm experimentally via sonomicrometry.

2.1. Phantom fabrication

Four *in vitro* phantoms mimicking the carotid artery were constructed using a water solution of 13% (mass%) polyvinyl alcohol (PVA) (Sigma–Aldrich, St. Louis, MO, US) and 1% (mass%) graphite powder with particle size < 50 μm (Merck KGaA, Darmstadt, Germany) similar to a previously described procedure [31]. The solution was heated with temperatures kept below 100 °C and stirred until it was fully dissolved. Thereafter, it was poured into an acrylic mold with a drilled cylindrical hole (diameter of 12 mm) in the middle of the mold representing the outer diameter of the vessel. The lumen was created by inserting a uniform metallic rod with a diameter of 6 mm in the middle of the 12 mm hole, which resulted in a phantom wall thickness of 3 mm. At each end of the phantom, fixing collars with an outer diameter of 28 mm were formed. Moreover, the mold was cut longitudinally in the center and axially at a distance of 20 mm from one of the extremities, to allow for extraction of the phantom from the mold. The parts were then kept together by screws while manufacturing the phantoms. Fig. 1a and b illustrate the geometry of the phantom and show a photo of one of the phantoms used in the study.

The mold containing the PVA/graphite solution was first stored in a freezer for 12 h (≈ −20 °C) and then thawed in room temperature (≈ 20 °C) for 12 h, which completed one freeze–thaw cycle. The number of applied freeze–thaw cycles determined the elasticity of the phantom, i.e. a large number of cycles resulted in a low elasticity and vice versa. The four phantoms were constructed using 2, 3, 3 and 4 freeze–thaw cycles, respectively, to obtain phantoms with different mechanical properties [34] and a range of strain amplitudes for the validation.

At completion of all freeze–thaw cycles, the phantoms were mounted in a polyvinyl chloride (PVC) box (110 mm × 85 mm × 300 mm) by squeezing the fixing collars between two plastic disks as illustrated in Fig 1c. To avoid reflections from the PVC-box, the bottom and the sides of the box were covered with a 3 mm thick rubber layer. Further, a solution of 3% (mass%) Agar (Merck KGaA, Darmstadt, Germany) and 4% graphite powder with particle size < 50 μm (Merck KGaA, Darmstadt, Germany) was poured into the PVC-box up to a level approximately 10 mm above the vessel phantom to mimic surrounding tissue.

2.2. Experimental setup

The phantoms were connected to a pulsatile flow pump, CompuFlow 1000MR (Shelley Medical Imaging Technologies, Ontario, Canada) by attaching hose assemblies with an inner diameter of 6 mm to the plastic disks in the PVC-box, see Fig. 1c [31]. A photo of the experimental setup is shown in Fig. 2a. A pre-programmed carotid flow profile (75 cycles/min) with peak flows at 14, 21, 28 and 35 ml/s was generated by the pulsatile pump as shown in

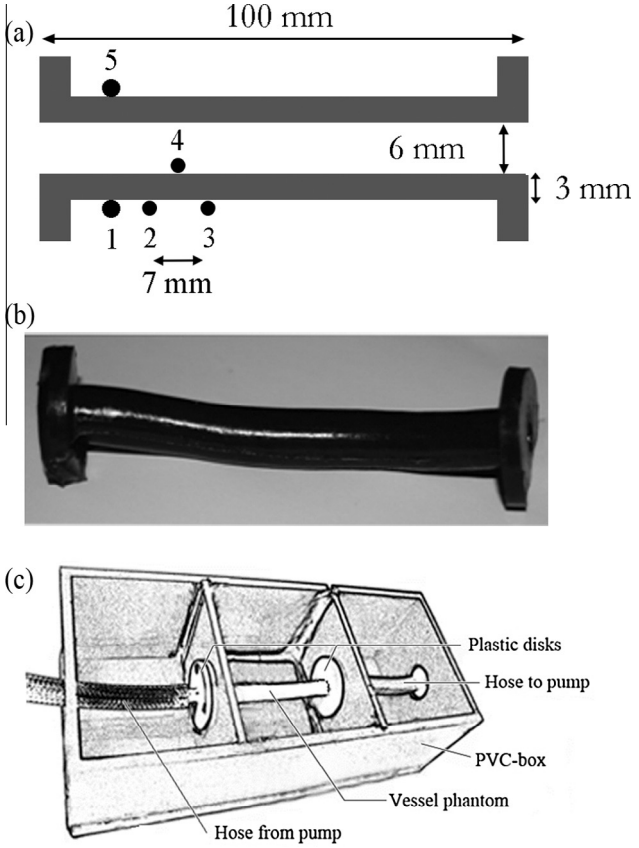

Fig. 1. The vessel phantom. (a) Schematic illustration showing the geometry of the vessel phantom and the positions of the sonomicrometry crystals (1–5). Crystals 2–4 had a diameter of 0.7 mm and crystal 1 and 5 of 1 mm. (b) Photo of the vessel phantom fabricated from a mixture of polyvinyl alcohol and graphite powder. (c) Illustration of the vessel phantom attached to the polyvinyl chloride (PVC) box [31].

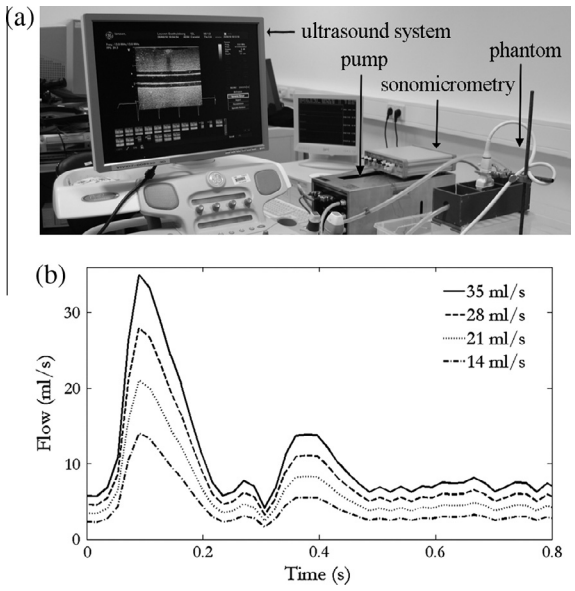

Fig. 2. (a) Experimental setup. Photo of the experimental setup using the Vivid 7 system for ultrasound imaging. (b) Flow profiles generated by the pulsatile pump at four different peak flows (14, 21, 28, 35 ml/s).

Fig. 2b. A solution of 40% glycerin (Acros Organics, Geel, Belgium) and 60% water was used to mimic the blood. Before starting the experiments, the pre-programmed drain procedure was performed to remove air bubbles from the blood mimicking fluid.

2.3. Data acquisition

Gray-scale ultrasound long- and short-axis images of the phantoms were obtained using a standard clinical ultrasound system, Vivid 7 (GE Healthcare, Horten, Norway) and a high-frequency ultrasound system, Vevo 2100 (FUJIFILM, VisualSonics, Toronto, Canada) with linear-array transducers fixed at the top of the phantom using a tripod holder. The scanning direction of the ultrasound transducers with respect to the flow in the phantoms was the same for every acquisition. The data from Vivid 7 will hereinafter be referred to as the clinical ultrasound images and the data from Vevo 2100 as the high-frequency ultrasound images. The imaging characteristics for both systems are presented in Table 1. Images were acquired throughout 3 pump cycles with the Vivid 7 system and throughout 1 pump cycle with the Vevo 2100 system. For both systems, the focus point was positioned in the far wall of the phantoms. Fig. 3 shows example gray-scale long- and short-axis images from one of the phantoms recorded by the two ultrasound systems.

Reference strain values were assessed using a sonomicrometry system at a sampling rate of 1063.8 Hz (Sonometrics, London, Ontario, Canada). Sonomicrometry crystals were glued to the phantom surface according to the illustration in Fig. 1a using cyanoacrylate glue (Super glue, Loctite, Düsseldorf, Germany). The crystals had a diameter of either 1 mm (crystal 1 and 5) or 0.7 mm (crystal 2, 3 and 4) depending on the inter-crystal displacement to be measured. The crystals that acquired data for reference circumferential strain (crystal 1 and 5) were glued on the outer surface of the phantom wall, 180° apart in the short-axis view. Crystal 2 and 3 were positioned close to crystal 1, approximately 7 mm apart longitudinally, to acquire data for longitudinal reference strain, whereas crystal 4 was glued on the inside of the phantom wall opposite crystal 2 and 3 to acquire data for radial strain calculation.

Sonomicrometry data and ultrasound images were acquired for all phantoms and flow profiles in randomized order. In order to avoid sound interference, the sonomicrometry system was switched off during ultrasound image acquisition and vice versa. Moreover, ultrasound imaging was performed parallel to the planes containing the sonomicrometry crystals to avoid crystal influence in the ultrasound images.

2.4. Data analysis

The collected data were analyzed offline using in-house developed Matlab (R2010a, MathWorks, Natick, MA, US) software [27] [31], in which the speckle tracking analysis was performed on the ultrasound images. Moreover, the inter-crystal distances were processed to assess reference strain values from the sonomicrometry data. The data were synchronized using a simulated ECG signal from the pump.

2.4.1. Speckle tracking analysis

Before applying the in-house speckle tracking algorithm, the Vevo 2100 data were downsampled with a factor of two, from 75 frames per second (fps) to 37.5 fps (i.e. every second image was selected) to resemble the frame rate of the data from the Vivid 7 system. Speckle tracking analysis was performed on the envelope detected data from the Vivid 7 system and on the radio-frequency (RF) data from the Vevo 2100 system using the previously developed algorithm [27]. In brief, speckles were tracked consecutively across frames in two directions (laterally; perpendicular to the beam, axially; along the beam) with a kernel size of 0.59 mm laterally and 0.24 mm axially, using normalized cross-correlation as

Table 1
Characteristics for standard clinical and high-frequency ultrasound imaging.

	System	Transducer	Transmitted frequency (MHz)	Frame rate (fps)	Image depth/width (mm)
Standard clinical ultrasound	Vivid 7	12L	12	43.2	30/27
High-frequency ultrasound	Vevo 2100	MS250	21	37.5[a]	30/14

fps; frames per second.
[a] Downsampled from 75 fps to 37.5 fps.

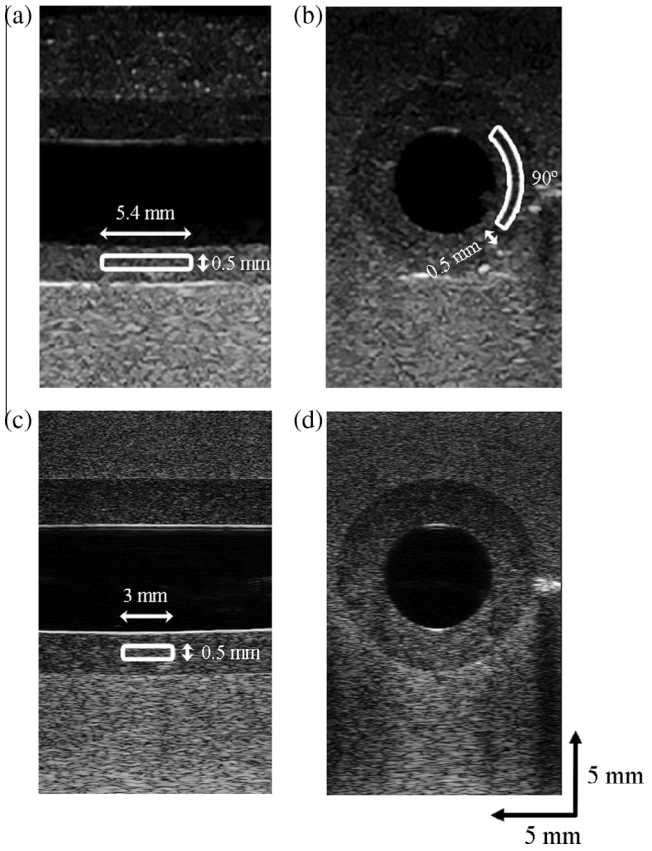

Fig. 3. Ultrasound sample images. Ultrasound long-axis (left) and short-axis (right) in end-diastole of a phantom constructed with 3 freeze–thaw cycles acquired by the clinical ultrasound system, Vivid 7 (a and b) and high-frequency system, Vevo 2100 (c and d). The white boxes represent the region of interest (ROI) for radial strain (c), longitudinal strain (a) and circumferential strain (b). The images have been slightly zoomed for better visualization of the phantom.

similarity measure. The kernels were slid over the image with 40% axial and lateral overlap and spline interpolation of the cross-correlation function was used to detect sub-sample motion. A 2D median filter was applied on a region of approximately 0.1 mm (axial) by 0.4 mm (lateral) to remove outliers, followed by linear interpolation between samples to obtain motion estimates in the entire image. Subsequently, the displacement maps were cumulated throughout each pump cycle using linear interpolation to account for sub-pixel motion.

In the long-axis views from both ultrasound systems, radial (i.e. perpendicular to the flow direction) and longitudinal strains (i.e. along the flow direction) were estimated throughout three and one pump cycle for the clinical and the high-frequency ultrasound system, respectively. Strains were estimated in a region of interest (ROI) manually positioned in the middle of the posterior vessel wall at a longitudinal distance of approximately 25 mm from the fixing collar of the phantom. The ROI width was 3 mm when calculating radial strains and 5.4 mm when calculating longitudinal strains whereas the ROI length was 0.5 mm for both radial and longitudinal strain estimation. The larger ROI width for longitudinal strain estimation than for radial strain estimation was chosen in order to partly compensate for the lower spatial resolution in the lateral direction of the image. Fig. 3 shows ultrasound gray-scale images from one of the phantoms with indicated ROIs for longitudinal (Fig. 3a) and radial (Fig. 3c) strain estimation.

In the short-axis views from both ultrasound systems, the lateral and axial displacement maps were converted into polar coordinates when calculating the circumferential strain. Strains were estimated throughout three and one pump cycle for the clinical and the high-frequency ultrasound system, respectively, in a circular ROI positioned in the middle of the phantom wall at 3 o'clock (radial ROI size = 0.5 mm, circumferential ROI size = 90°). Fig. 3 shows ultrasound gray-scale images from one of the phantoms with indicated ROI for circumferential strain estimation (Fig. 3b).

The strain values were obtained by spatial linear regression after averaging the cumulated displacement maps in one direction of the ROI (radially for longitudinal strain, longitudinally for radial strain and radially for circumferential strain). Finally, the estimated strain curves were drift compensated to obtain values of zero strain at the end of each pump cycle. The drift compensated strain (ε_{DC}) in frame t was calculated as:

$$\varepsilon_{DC}(t) = \varepsilon(t) - \frac{\sum_{i=1}^{t}|\varepsilon(i)-\varepsilon(i-1)|}{\sum_{j=1}^{T}|\varepsilon(j)-\varepsilon(j-1)|}\varepsilon(T) \quad (1)$$

where frame 1 was the first frame and frame T the last frame in the pump cycle. Subsequently, the strain curves were low-pass filtered in order to remove noise, by convolving the curves with a normalized rectangular function of 4 time samples in length.

2.4.2. Sonomicrometry

The inter-crystal displacement curves between crystal 1 and 5, crystal 2 and 3, crystal 2 and 4, and crystal 3 and 4 were median filtered with a filter length of 35 ms to reduce noise. Subsequently, the curves were averaged over six pump cycles. According to the law of cosines, the radial instantaneous length $D_R(t)$ was calculated as:

$$D_R(t) = D_{2-4}(t) \times \sin\left(a\cos\frac{D_{2-4}^2(t) + D_{2-3}^2(t) - D_{3-4}^2(t)}{2 \times D_{2-4}(t) \times D_{2-3}(t)}\right) \quad (2)$$

where $D_{2-3}(t)$ was the inter-crystal distance between crystal 2 and 3 at time point t, i.e. the longitudinal stretching $D_L(t)$, $D_{2-4}(t)$ between crystal 2 and 4 and $D_{3-4}(t)$ between crystal 3 and 4. The circumferential stretching $D_C(t)$ in the middle of the wall equaled the distance between crystal 1 and 5 subtracted by $D_R(t)$. The radial (R), longitudinal (L) and circumferential (C) strain (ε) was then calculated throughout one pump cycle as:

$$\varepsilon_i(t) = \left(\frac{D_i(t) - D_i(t_o)}{D_i(t_o)}\right) \quad (3)$$

where $D_i(t_0)$ was the inter-crystal displacement at the start of the pump cycle and $D_i(t)$ the inter-crystal displacement at time point t with $i = R, L, C$.

2.4.3. Statistical analysis

The peak radial, longitudinal and circumferential strains were identified in the strain curves obtained by speckle tracking and sonomicrometry. It should be noted that peak radial strains were negative, whereas longitudinal and circumferential peak strains were positive. Estimated peak strains were correlated with reference peak strains obtained by sonomicrometry using the Pearson correlation coefficient. For peak strain values obtained from Vivid 7 data, both the peak value from the first cycle and the peak strain averaged over three cycles were used in the correlation analysis. The data were also processed in a Bland–Altman analysis, where the bias in the strain estimation was calculated as the difference between the estimated and reference peak strain values ($\hat{\varepsilon}_{peak} - \varepsilon_{peak}$) averaged over all phantoms and flows. A paired *t*-test was used to test if there was a significant bias in the estimations and if the difference in bias between estimation on clinical and high-frequency ultrasound data was significant. The root mean square error (RMSE) between reference and estimated strains throughout one pump cycle was calculated as:

$$RMSE = \sqrt{\sum_{t=1}^{N} \frac{(\varepsilon(t) - \hat{\varepsilon}(t))^2}{T}} \quad (4)$$

where $\hat{\varepsilon}(t)$ was the estimated strain, $\varepsilon(t)$ the reference strain and T the number of frames in one pump cycle. Only the first pump cycle for the estimation based on clinical ultrasound data was selected for RMSE calculation. A paired *t*-test was used to test if the RMSE significantly differed between estimation on clinical and high-frequency ultrasound data. *P*-values lower or equal to 0.05 were considered significant.

Moreover, the variability in peak strain values over time was calculated as the relative mean difference (RMD) between the three peak strain values obtained from estimation based on the clinical ultrasound data as:

$$RMD = \frac{(|\hat{\varepsilon}_1 - \hat{\varepsilon}_2| + |\hat{\varepsilon}_1 - \hat{\varepsilon}_3| + |\hat{\varepsilon}_2 - \hat{\varepsilon}_3|)}{3 \times \varepsilon} \times 100 \quad (5)$$

where $\hat{\varepsilon}_{1-3}$ was the estimated peak strain for each of the three pump cycles and ε the peak reference strain.

3. Results

The strain curves estimated by the speckle tracking algorithm cyclically varied over time, showing a radial compression (negative strain), a circumferential stretching (positive strain) and a longitudinal stretching (positive strain) in the first half of the pump cycle mimicking the cardiac systole. Overall, the estimated strain corresponded well with the reference strain acquired with sonomicrometry. Example strain curves throughout three pump cycles from estimation on clinical ultrasound data and sonomicrometry in two of the phantoms (3 freeze–thaw cycles) are shown in Fig. 4.

Fig. 5 shows correlation (Fig. 5a–c) and Bland–Altman plots (Fig. 5d–f) based on peak strain estimation on the clinical ultrasound data averaged over three pump cycles, whereas Fig. 6 shows correlation plots (Fig. 6a–c) and Bland–Altman plots (Fig. 6d–f) based on peak strain estimation on data acquired by the high-frequency ultrasound system throughout one pump cycle.

Table 2 presents bias, RMD and RMSE from strain estimation on images obtained by the clinical and high-frequency ultrasound system for radial, longitudinal and circumferential strain estimation. The peak circumferential strain was slightly underestimated when using the clinical ultrasound system ($p < 0.05$), whereas no significant bias was found in the estimation of peak radial and longitudinal strain. The variability of peak strain estimation based on data from the clinical ultrasound system over the three cardiac cycles expressed as RMD varied between 19.87% and 31.97% for the three estimation directions.

When comparing speckle tracking performance on the clinical and high-frequency ultrasound data, only strain curves from the first pump cycle from the estimation on clinical data were considered. This was done because the Vevo 2100 system only allowed acquisition of one pump cycle due to limitations in storage capacity. When considering only the first pump cycle, the estimation based on clinical ultrasound data resulted in a correlation coefficient between estimated peak strain and reference strain of 0.86 ($p < 0.001$) for radial strain, 0.70 ($p < 0.01$) for longitudinal strain and 0.83 ($p < 0.001$) for circumferential strain (not shown in figure). When estimating circumferential strain, a significant difference in bias and RMSE was found between estimation on clinical and high-frequency ultrasound data (see Table 2), showing a larger bias and RMSE for the estimation based on data from the clinical ultrasound system. No significant difference in bias and RMSE was found between radial and longitudinal strain estimation on ultrasound images acquired by the clinical and high-frequency ultrasound system.

4. Discussion

In this study, radial, longitudinal and circumferential strain estimation of the carotid artery, by speckle tracking using a clinical and high-frequency ultrasound system, was validated in an experimental setup via sonomicrometry. In general, good agreement was found between ultrasound speckle tracking and sonomicrometry strain which indicates the feasibility of carotid strain estimation using ultrasound speckle tracking. These results are consistent with previous studies reporting the feasibility to estimate strain of the carotid artery *in silico* [17,27,35], *in vitro* [17,18] and *in vivo* [36]. However, most studies have focused on radial and circumferential strain assessment and experimental validation of arterial strain in three directions via an independent method has to the authors' knowledge only been presented in our preliminary *in vitro* study using clinical ultrasound in a smaller set of phantoms.

The bias and RMSEs found in this study were overall larger than in our previous *in silico* study in which the performance of the speckle tracking algorithm was assessed on simulated two-dimensional ultrasound images of a cylindrical carotid artery model [27]. The larger errors in this study may be the result of a validation setting that was more similar to the *in vivo* setting, inducing a larger amount of noise and imaging artifacts. Furthermore, the use of sonomicrometry compared with the ground truth of the model most probably resulted in larger discrepancies between estimation and reference. The spatial resolution of the sonomicrometry system was 15.4 μm with an absolute accuracy of 250 μm, which corresponded to ¼ wavelength of the transmitted ultrasound.

4.1. Strain estimation on the standard clinical ultrasound data

The *in vitro* validation based on clinical ultrasound data showed strong significant correlations with sonomicrometry when estimating peak radial ($r = 0.91$) and circumferential ($r = 0.90$) strain averaged over three pump cycles. The correlation between estimated and reference peak longitudinal strain ($r = 0.73$) was weaker but still sufficient to demonstrate correlation between the methods. As demonstrated in the Bland–Altman plots (Fig. 5), speckle tracking showed a tendency to overestimate radial strain, whereas both longitudinal and circumferential strains were underestimated. However, the bias was only significant for circumferential strain estimation ($p < 0.001$), which may be related to the fact that the phantoms were positioned in an open box with different

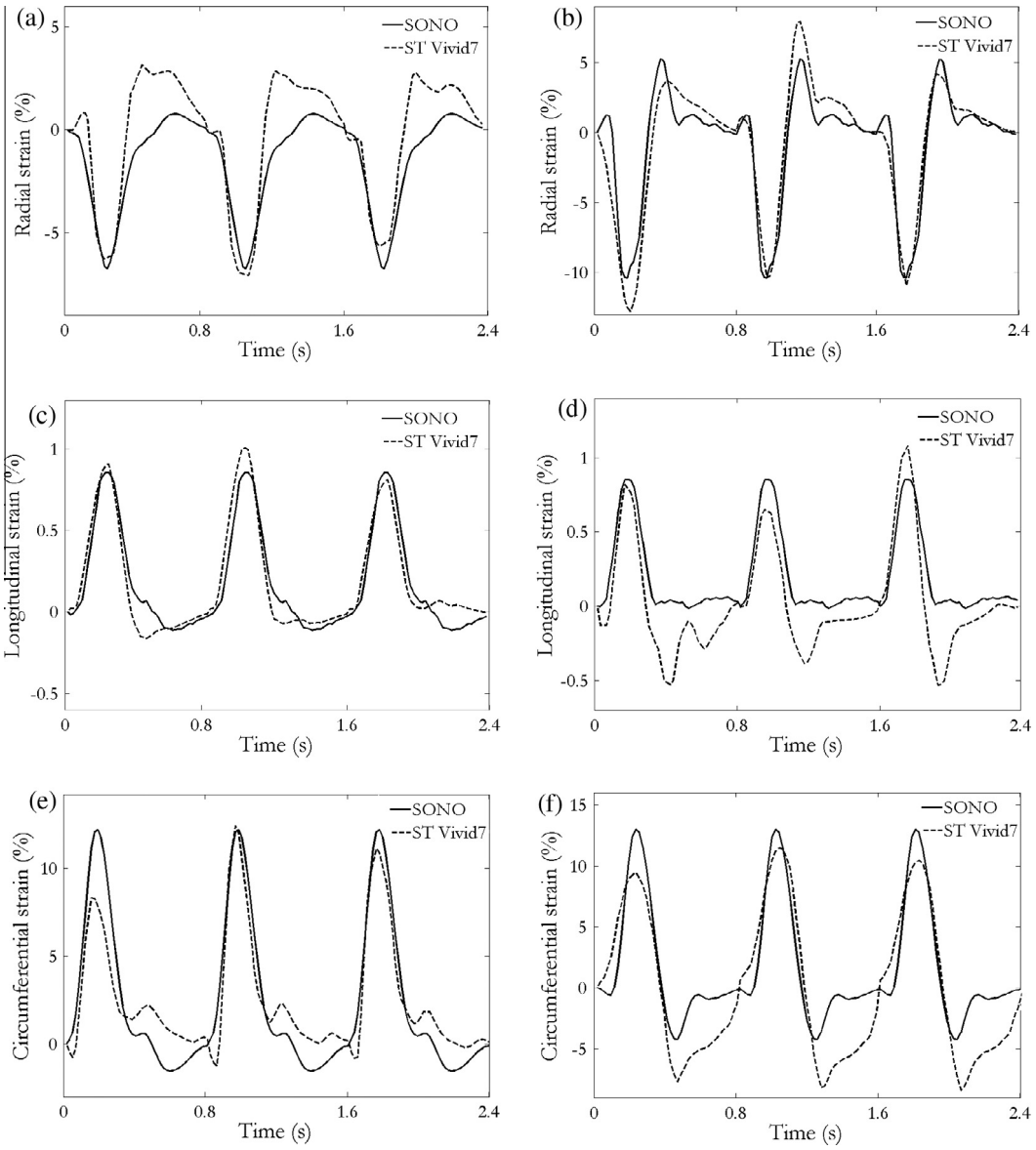

Fig. 4. Strain estimation sample curves. Radial strain (upper plots), longitudinal strain (mid plots) and circumferential strain (lower plots) from three consecutive pump cycles estimated by ST using the clinical ultrasound system (Vivid 7) and reference strain by SONO in two (a and b) polyvinyl alcohol phantoms (3 freeze–thaw cycles) at a peak flow of 35 ml/s. ST; speckle tracking, SONO; Sonomicrometry.

surrounding conditions at the top and bottom and that circumferential reference strain was assessed from diameter change and thus dependent on movement of both the near and far wall of the phantom. The difference in boundary conditions may have influenced the estimation in the circumferential direction more than in the radial and longitudinal direction, since the discrepancy in measurements sites for speckle tracking and sonomicrometry was larger for circumferential strain than for radial and longitudinal strain, which both were assessed in the far wall of the phantoms. Moreover, the relative small RMD in the circumferential direction may be a proof of reliable measurements whereas the relative large bias indicates that the slightly different measurement sites influenced the comparison of estimated and reference strain.

Further, the limits of agreement related to the estimated strain amplitude were lower in the radial and circumferential direction than for longitudinal strain estimation. The lower lateral resolution and small lateral displacements in relation with the wavelength of the applied ultrasound were most likely causes of the weaker correlation and larger limits of agreement for longitudinal strain estimation compared with estimation in the radial and circumferential dimension. However, since a lower accuracy was expected longitudinally, a larger motion gradient estimation length was used in the lateral direction to in some extent compensate for the lower lateral resolution. However, this could apparently not fully compensate for this effect.

The pulsatile pump performed a reproducible inflow profile to the phantoms over time imposing a low variability in phantom peak strain over consecutive pump cycles. However, a relative high variability in estimated peak strain values ($20\% < RMD < 32\%$) over consecutive pump cycles was obtained in the clinical ultrasound data set. Moreover, the variability in strain values over consecutive pump cycles was higher for longitudinal strain estimation than for radial and circumferential strain estimation, which also indicates that longitudinal strain estimation is more challenging. This stresses the importance of repeated measurements in future studies when assessing arterial strain *in vivo*. Most probable, the *in vivo*

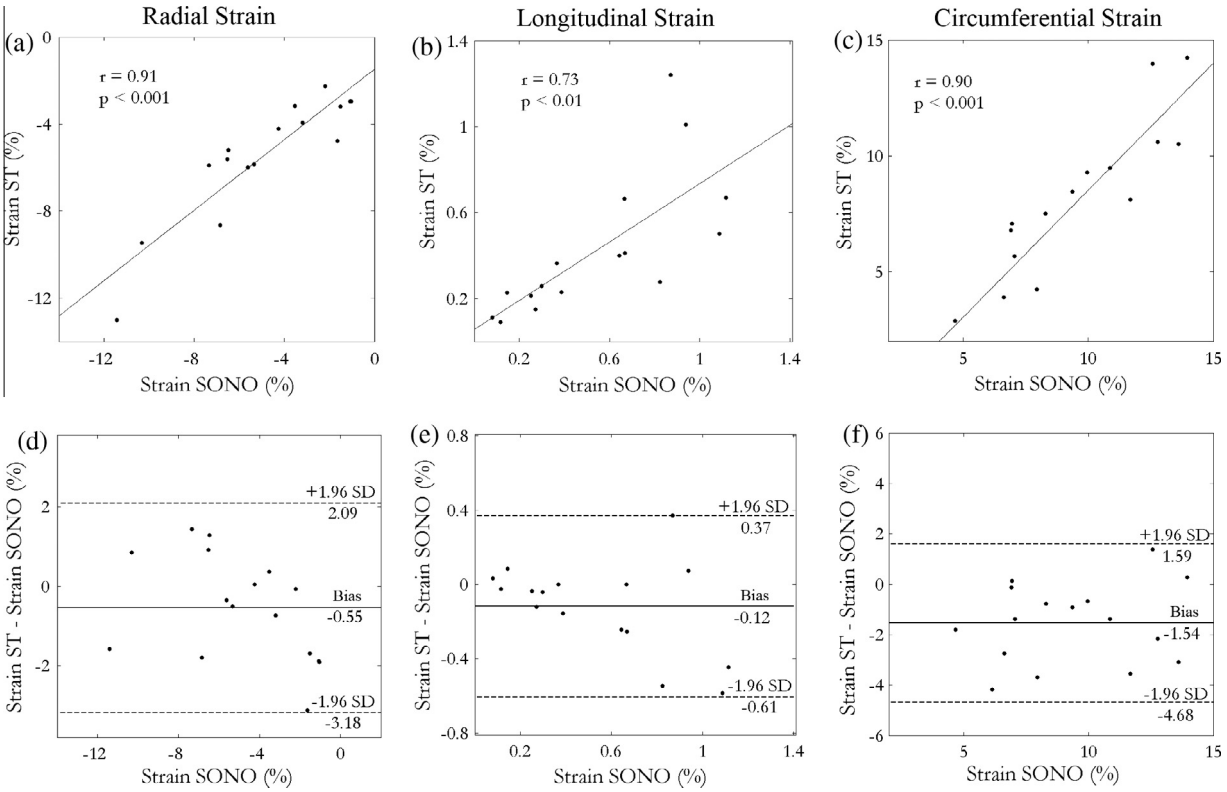

Fig. 5. Strain estimation results on the clinical ultrasound data (Vivid7). The data represent three pump cycles in four PVA-phantoms at peak flows of 14, 21, 28 and 35 ml/s. (a–c) Correlation plots of peak radial, longitudinal and circumferential strain by ST (mean of three pump cycles) and strain by SONO. The linear regression line, correlation coefficient (r) and significance level (p) are shown in the plots. (d-f) Bland-Altman plots of peak radial, longitudinal and circumferential strain by ST (mean of three pump cycles) and SONO. The mean (bold line) and limits of agreement (±1.96 SD, dashed lines) have been marked in the plots. ST; speckle tracking, SONO; sonomicrometry, PVA; polyvinyl alcohol, SD; standard deviation.

setting further increases the demand of repeated measurements, since e.g. breathing and unstable transducer placement may lead to out-of-plane motions and speckle decorrelation. In a clinical application, measurements throughout several cardiac cycles would be preferable to allow cycles with large variation in strain amplitude to be excluded from the analysis.

To demonstrate the clinical applicability of the presented speckle tracking algorithm, the accuracy of the method has to be related to clinical relevant differences in arterial strain values. According to previous studies, a difference of approximately 4% in circumferential strain was observed between young and old healthy subjects [36,37], whereas radial strain differed up to 10% between patients with coronary artery disease and healthy control subjects [20]. Although these studies were performed with other ultrasound systems and speckle tracking algorithms and furthermore limited to small patient populations, these findings indicate that the proposed algorithm in this study may have potential to detect clinical relevant differences in radial strain, whereas the limits of agreement for circumferential strain were slightly higher than the difference observed between young and old healthy subjects. However, the difference in circumferential strain between healthy and diseased subjects needs to be further investigated.

4.2. Comparison of strain estimation on the clinical and high-frequency ultrasound

This study also investigated if the use of a high-frequency ultrasound system could improve arterial speckle tracking performance because of e.g. increased spatial resolution. In this case, an improvement in lateral resolution could be expected and thus a longitudinal strain estimation of higher accuracy. The correlation coefficient of peak longitudinal strain increased from $r = 0.70$ to $r = 0.93$, which indicates an improved estimation in the longitudinal direction when applying the speckle tracking algorithm on ultrasound data obtained by the high-frequency ultrasound system compared with the clinical system. Also the limits of agreements for longitudinal strain estimation were slightly lower when using the high-frequency data compared with the clinical data. However, the longitudinal bias did not significantly decrease when using high-frequency ultrasound.

Similar results as for longitudinal strain estimation were obtained for radial strain estimation, when comparing estimation based on the clinical and high-frequency ultrasound data. The correlation coefficient and bias slightly improved but no significant difference in bias was obtained. On the contrary, a significant decrease in bias magnitude was found for circumferential strain estimation when using the high-frequency ultrasound system, which may be a result of the improved lateral resolution since circumferential strain estimation relies on both lateral and axial estimation when converting the motion estimates into polar coordinates. A possible reason why circumferential and not longitudinal strain estimation improved with increased spatial resolution may be the difference in amplitude values. Longitudinal peak strain values were lower (<1.5%) than circumferential peak strain values (<15%), imposing low inter-frame displacements close to sub-pixel level, which are difficult to track. As a result, the improved lateral resolution may have had a larger influence when estimating circumferential strain. This was also reflected in the RMSE, which was significant lower only in the circumferential direction, see rightmost column in Table 2.

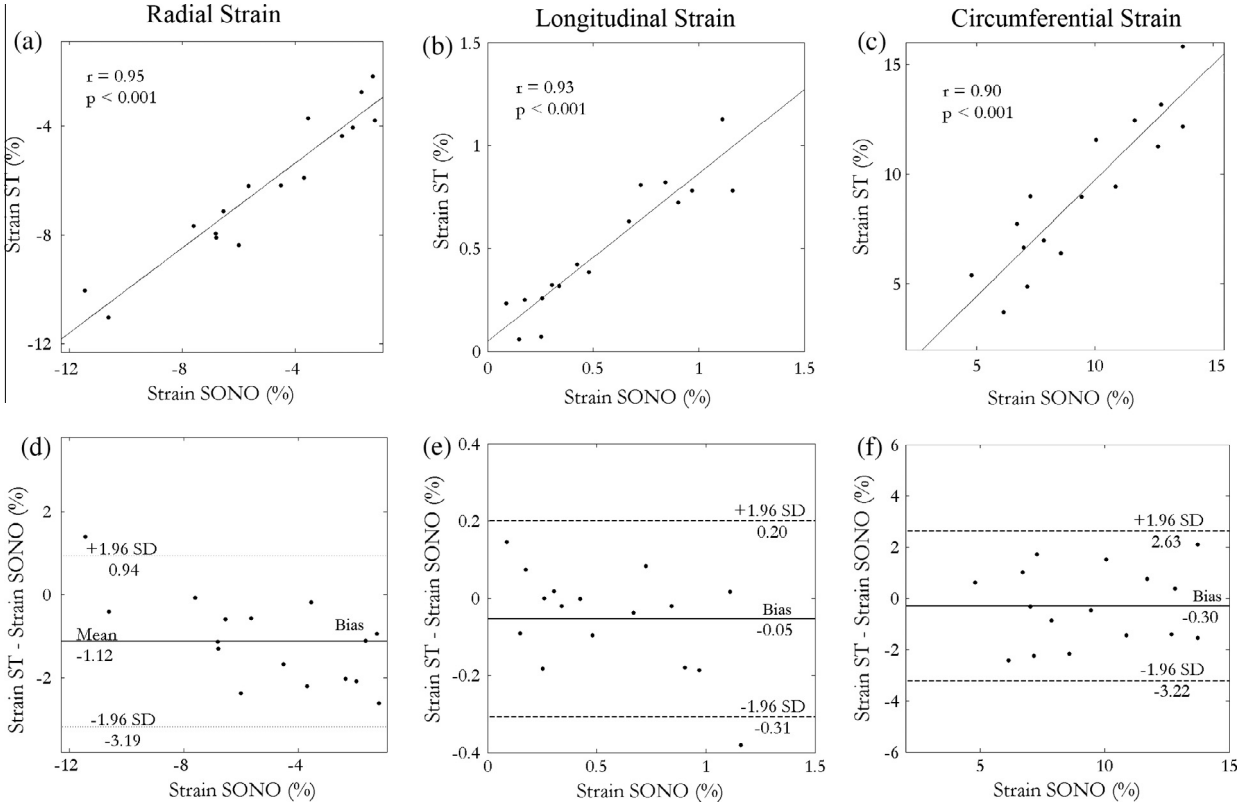

Fig. 6. Strain estimation results on the high-frequency ultrasound data (Vevo 2100). The data represent one pump cycle in four PVA-phantoms at peak flows of 14, 21, 28 and 35 ml/s. (a–c) Correlation plots of peak radial, longitudinal and circumferential strain by ST and strain by SONO. The linear regression line, correlation coefficient (r) and significance level (p) are shown in the plots. (d–f) Bland Altman plots of peak radial, longitudinal and circumferential strain by ST and SONO. The mean (bold line) and limits of agreement (±1.96 SD, dashed lines) have been marked in the plots. ST; speckle tracking, SONO; sonomicrometry, PVA; polyvinyl alcohol, SD; standard deviation.

Table 2
Strain estimation results. The data represent speckle tracking strain estimation on images acquired with the clinical ultrasound system, Vivid 7 (one pump cycle and mean over three pump cycles) and high-frequency ultrasound system, Vevo 2100 (one pump cycle) in four phantoms at four different peak flows (n = 16). Bias, RMD (Eq. (5)) and RMSE (Eq. (4)) for radial, longitudinal and circumferential strain estimation are presented as mean values ± SD. The bias differed significantly from zero only for the circumferential strain estimation on the clinical ultrasound data. The difference (Δ) in bias and RMSE (Eq. (5)) between estimation on clinical and high-frequency ultrasound data for radial, longitudinal and circumferential strain estimation throughout one pump cycle are presented as mean values ± SD in the right most column. Significant difference was found only when comparing bias and RMSE for circumferential strain estimation. The levels of significance have been marked by stars. RMD; relative mean difference, RMSE; root mean square error, SD; standard deviation.

	Vivid 7 *mean of 3 cycles*	Vivid 7 *1 cycle*	Vevo 2100 *1 cycle*	Δ (Vivid 7 – Vevo 2100) *1 cycle*
Radial strain				
Bias (%)	−0.55 (1.34)	−0.31 (1.05)	−1.12 (1.05)	0.81 (1.66)
RMD (%)	25.93 (20.69)	–	–	–
RMSE (%)	–	2.35 (1.55)	1.79 (0.81)	0.56 (1.80)
Longitudinal strain				
Bias (%)	−0.12 (0.25)	−0.14 (0.17)	−0.05 (0.13)	−0.09 (0.27)
RMD (%)	31.97 (27.75)	–	–	–
RMSE (%)	-	0.26 (0.13)	0.21 (0.12)	0.05 (0.13)
Circumferential strain				
Bias (%)	−1.54 (1.60) [b]	−1.70 (1.82)[a]	−0.30 (1.49)	−1.41 (2.52)[a]
RMD (%)	19.87 (11.97)	–	–	–
RMSE (%)	–	3.46 (1.20)	2.76 (1.43)	0.70 (1.20)[a]

[a] $p < 0.05$.
[b] $p < 0.001$.

In general, the strain estimation results were slightly better when applying the speckle tracking algorithm on data from the high-frequency system compared with the clinical system, even though the estimation was significantly improved only in the circumferential direction. This implies that an increase in transmitted ultrasound frequency from 12 MHz to 21 MHz is not sufficient to highly improve the accuracy of the speckle tracking algorithm. As such, both systems can be used nearly interchangeable in the arterial strain application. However, other factors that could have influenced the strain estimation performance might be differences in filters and other image processing features between the two systems that could not be controlled in this study. The imaging parameters of the Vivid 7 system were chosen according to the previous *in silico* study in which this system using a 12L linear

array transducer was simulated [27]. The imaging parameters for acquisition of the high-frequency data sets were chosen to resemble the setting of the clinical system. However, equivalent imaging setups were not obtained due to limitations in possible parameter selections by the user. As such, only one pump cycle could be stored for the Vevo 2100 system and the frame rate had to be downsampled to be in the same range as for the Vivid 7 system. Still, the frame rates were not precisely corresponding which could have influenced the tracking results. Furthermore, speckle tracking was performed on envelope-detected data from the Vivid 7 system whereas the data from the Vevo 2100 system were RF-data, which may have been an advantage for the estimation on high-frequency data. However, our previous study demonstrated no significant difference when estimating arterial strain on envelope-detected data and RF-data when transmitting the same center frequency [27].

4.3. Limitations

This study was limited to an experimental validation setup and the feasibility of ultrasound speckle tracking for carotid strain assessment needs to be further investigated *in vivo*. The vessel phantoms were manufactured with appropriate geometry and mechanical and acoustical tissue properties to mimic the common carotid artery [34]. Still, the strain values in this study differed from those previously reported *in vivo* [20,36], in particular the longitudinal ones, which were lower compared with strain values observed *in vivo* [38]. The fixation at each end of the phantom restricted the longitudinal movement, which could probably have been avoided by letting one end of the phantom freely move. In addition, the range of peak flows included lower peak flows than normally observed *in vivo* to get a wider range of values for the correlation analysis. Furthermore, the wall thickness of the vessel phantom was 3 mm, which is larger than the intima media thickness of a human carotid artery [3]. However, to fabricate a phantom with a thinner vessel wall was difficult to realize. Instead, to mimic strain assessment in the human carotid artery, the ROI length was kept small (0.5 mm) and the ROI was placed in the center of the phantom wall. In addition, the three layers of the artery and their different mechanical properties and geometry may affect the performance of the speckle tracking algorithm in *in vivo* applications. Also, the circumferential strain may be more difficult to estimate *in vivo* due to asymmetries of the artery in the short-axis view.

Both sonomicrometry and speckle tracking strain estimation might have induced errors. A common source of error in ultrasound-based strain estimation is speckle decorrelation due to tissue compression and out-of-plane motion. Moreover, the use of sonomicrometry as reference method can be questioned, since its accuracy is limited in terms of spatial resolution when measuring such small distances. Another factor that could have influenced the discrepancy between the methods was slightly different measurement sites, which was necessary in order to avoid interference of the crystals in the tracking process and also a result of manual placement of the ultrasound transducer. Moreover, to avoid sound interference, the sonomicrometry and ultrasound system did not operate simultaneously. However, as already mentioned the pump achieved a stable movement pattern of the phantom over consecutive pump cycles, which allowed for accurate temporal alignment of ultrasound and crystal data using the simulated ECG-signal from the pump.

4.4. Future perspectives

An accurate method allowing for arterial strain assessment has potential to be used in the clinical setting providing measures of arterial stiffness and plaque vulnerability. In a broader perspective, an accurate method for arterial strain assessment could help to increase the general understanding of the cardiovascular system. The literature lacks on larger studies reporting arterial strain values *in vivo*, especially longitudinal strain values. The number of studies describing longitudinal strain of the arterial wall is currently limited and further research is required to determine the clinical value of arterial longitudinal motion and strain estimations although it has been shown that the longitudinal motion of the artery may be an important factor in early detection of cardiovascular diseases [39]. Recent findings also associate reduced longitudinal artery wall motion with plaque burden [29] and potential to predict cardiovascular outcome [40], which indicates that the arterial longitudinal function is an important contributor in the evaluation of cardiovascular diseases.

The presented validation setup can be used for future improvements of speckle tracking algorithms applied on the arterial wall, e.g. development of speckle tracking applied on three-dimensional vascular data sets. Additionally, it would be of interest to further validate the algorithm via invasive measurements in experimental animal models and atherosclerotic plaque models to further mimic the setting in clinical practice. The *in vivo* setting is however challenging given that more motion artifacts due to e.g. breathing are present. Moreover, further studies are needed to test the feasibility of this algorithm in large patient populations in order to understand the strain pattern of the carotid artery *in vivo*, its dependence on e.g. age, gender and disease and to determine the clinical value and importance of carotid strain in the estimation of arterial stiffness and characterization of atherosclerotic plaques.

5. Conclusions

This study demonstrates that radial, longitudinal and circumferential strain assessment of the carotid artery wall is feasible when applying speckle tracking on ultrasound data sets of gel phantoms acquired by a clinical and high-frequency ultrasound system. The speckle tracking performance was not considerably improved when applied on data from the high-frequency ultrasound system compared with the clinical ultrasound system. Further studies are needed to validate the algorithm on *in vivo* data and to investigate the potential of the method to estimate arterial stiffness and characterize atherosclerotic plaques.

Acknowledgement

This study was supported by VINNOVA VINNMER Marie Curie International qualification (2011-01365), Swedish Research Council (2012-2795), Swedish Heart-Lung Foundation (20090896), Research Foundation Flanders (FWO) – Flanders grant G.0684.08 and Swedish Stroke Foundation. The Vevo 2100 system used in this study was available through funding of the Hercules Foundation Flanders.

References

[1] K. Sutton-Tyrrell, S. Najjar, R. Boudreau, L. Venkitachalam, V. Kupelian, E. Simonsick, R. Havlik, E. Lakatta, H. Spurgeon, S. Kritchevsky, M. Pahor, D. Bauer, A. Newman, Elevated aortic pulse wave velocity, a marker of arterial stiffness, predicts cardiovascular events in well-functioning older adults, Circulation 111 (2005) 3384–3390.

[2] M. Naghavi, P. Libby, E. Falk, S.W. Casscells, S. Litovsky, J. Rumberger, J.J. Badimon, C. Stefanadis, P. Moreno, G. Pasterkamp, Z. Fayad, P.H. Stone, S. Waxman, P. Raggi, M. Madjid, A. Zarrabi, A. Burke, C. Yuan, P.J. Fitzgerald, D.S. Siscovick, C.L. de Korte, M. Aikawa, K.E. Juhani Airaksinen, G. Assmann, C.R. Becker, J.H. Chesebro, A. Farb, Z.S. Galis, C. Jackson, I.K. Jang, W. Koenig, R.A. Lodder, K. March, J. Demirovic, M. Navab, S.G. Priori, M.D. Rekhter, R. Bahr, S.M. Grundy, R. Mehran, A. Colombo, E. Boerwinkle, C. Ballantyne, W. Insull, Jr., R.S. Schwartz, R. Vogel, P.W. Serruys, G.K. Hansson, D.P. Faxon, S. Kaul, H. Drexler, P. Greenland, J.E. Muller, R. Virmani, P.M. Ridker, D.P. Zipes, P.K. Shah, J.T. Willerson, From vulnerable plaque to vulnerable patient: a call for new definitions and risk assessment strategies: Part I, Circulation 108 (2003) 1664–1672.

[3] M. Bots, J. Witteman, D. Grobbee, Carotid intima-media wall thickness in elderly women with and without atherosclerosis of the abdominal aorta, Atherosclerosis 102 (1993) 99–105.
[4] E. Hermeling, K. Reesink, R. Reneman, A. Hoeks, Measurement of local pulse wave velocity: effects of signal processing on precision, Ultrasound Med. Biol. 33 (2007) 774–781.
[5] A. Redheuil, Y. Wen-Chung, C. Wu, E. Mousseaux, A. de Cesare, R. Yan, N. Kachenoura, D. Bluemke, J. Lima, Reduced ascending aortic strain and distensibility: earliest minifestations of vascular aging in humans, Hypertension 55 (2010) 319–326.
[6] A. Hoeks, P. Brands, F. Smeets, R. Reneman, Assessment of the distensibility of superficial arteries, Ultrasound Med. Biol. 16 (1990) 121–128.
[7] N.K. Eryol, R. Topsakal, Y. Çiçek, A. Abaci, A. Oguzhan, E. Basar, A. Ergin, Color doppler tissue imaging in assessing the elastic properties of the aorta and in predicting coronary artery disease, Jpn. Heart J. 43 (2002) 219–230.
[8] M. Couade, M. Pernot, C. Prada, E. Messas, J. Emmerich, P. Bruneval, A. Criton, M. Fink, M. Tanter, Quantitative assessment of arterial wall biomechanical properties using shear wave imaging, Ultrasound Med. Biol. 36 (2010) 1662–1676.
[9] J.M. Wardlaw, F.M. Chappell, J.J. Best, K. Wartolowska, E. Berry, N.H.S. Research, G. Development Health Technology Assessment Carotid Stenosis Imaging, Non-invasive imaging compared with intra-arterial angiography in the diagnosis of symptomatic carotid stenosis: a meta-analysis, Lancet, 367 (2006) 1503–1512.
[10] D. Staub, A.F. Schinkel, B. Coll, S. Coli, A.F. van der Steen, J.D. Reed, C. Krueger, K.E. Thomenius, D. Adam, E.J. Sijbrands, F.J. ten Cate, S.B. Feinstein, Contrast-enhanced ultrasound imaging of the vasa vasorum: from early atherosclerosis to the identification of unstable plaques, JACC Cardiovasc. Imaging. 3 (2010) 761–771.
[11] M. Fleiner, M. Kummer, M. Mirlacher, G. Sauter, G. Cathomas, R. Krapf, B.C. Biedermann, Arterial neovascularization and inflammation in vulnerable patients: early and late signs of symptomatic atherosclerosis, Circulation 110 (2004) 2843–2850.
[12] E. Falk, P.K. Shah, V. Fuster, Coronary plaque disruption, Circulation 92 (1995) 657–671.
[13] P. Prati, A. Tosetto, M. Casaroli, A. Bignamini, L. Canciani, N. Bornstein, G. Prati, P.J. Touboul, Carotid plaque morphology improves stroke risk prediction: usefulness of a new ultrasonographic score, Cerebrovasc. Dis. 31 (2011) 300–304.
[14] R. Topakian, A. King, S.U. Kwon, A. Schaafsma, M. Shipley, H.S. Markus, Ultrasonic plaque echolucency and emboli signals predict stroke in asymptomatic carotid stenosis, Neurology 77 (2011) 751–758.
[15] J. D'hooge, E. Konofagou, F. Jamal, A. Heimdal, L. Barrios, B. Bijnens, J. Thoen, F. Van de Werf, G. Sutherland, P. Suetens, Two-dimensional ultrasonic strain rate measurement of the human heart In Vivo, IEEE Trans. Ultrason. Ferroelectr. Freq. Control 49 (2002) 281–286.
[16] C.L. de Korte, H.H. Hansen, A.F. van der Steen, Vascular ultrasound for atherosclerosis imaging, Interf. Focus 1 (2011) 565–575.
[17] H.H. Hansen, R.G. Lopata, C.L. de Korte, Noninvasive carotid strain imaging using angular compounding at large beam steered angles: validation in vessel phantoms, IEEE Trans. Med. Imaging 28 (2009) 872–880.
[18] H. Ribbers, R. Lopata, S. Holewijn, G. Pasterkamp, J. Blankensteijn, C. de Korte, Noninvasive two-dimensional Strain Imaging of arteries: validation in phantoms and preliminary experience in carotid arteries in vivo, Ultrasound Med. Biol. 33 (2007) 530–540.
[19] M. Catalano, A. Lamberti-Castronuovo, A. Catalano, D. Filocamo, C. Zimbalatti, Two-dimensional speckle-tracking strain imaging in the assessment of mechanical properties of carotid arteries: feasibility and comparison with conventional markers of subclinical atherosclerosis, Eur J Echocardiogr. 12 (2011) 528–535.
[20] T. Kawasaki, S. Fukuda, K. Shimada, K. Maeda, K. Yoshida, H. Sunada, H. Inanami, H. Tanaka, S. Jissho, H. Taguchi, M. Yoshiyama, J. Yoshikawa, Direct measurement of wall stiffness for carotid arteries by ultrasound strain imaging, J. Am. Soc. Echocardiogr. 22 (2009) 1389–1395.
[21] Y. Liang, H. Zhu, M.H. Friedman, The correspondence between coronary arterial wall strain and histology in a porcine model of atherosclerosis, Phys. Med. Biol. 54 (2009) 5625–5641.
[22] C.L. de Korte, M.J. Sierevogel, F. Mastik, C. Strijder, J.A. Schaar, E. Velema, G. Pasterkamp, P.W. Serruys, A.F. van der Steen, Identification of atherosclerotic plaque components with intravascular ultrasound elastography in vivo: a Yucatan pig study, Circulation 105 (2002) 1627–1630.
[23] S. Korukonda, M.M. Doyley, Visualizing the radial and circumferential strain distribution within vessel phantoms using synthetic-aperture ultrasound elastography, IEEE Trans. Ultrason. Ferroelectr. Freq. Control 59 (2012) 1639–1653.
[24] M. McCormick, T. Varghese, X. Wang, C. Mitchell, M.A. Kliewer, R.J. Dempsey, Methods for robust in vivo strain estimation in the carotid artery, Phys. Med. Biol. 57 (2012) 7329–7353.
[25] C. Schmitt, G. Soulez, R. Maurice, M. Giroux, G. Cloutier, Noninvasive vascular elastography: toward a complementary characterization tool of atherosclerosis in carotid arteries, Ultrasound Med. Biol. 33 (2007) 1841–1858.
[26] M. Cinthio, Å. Rydén Ahlgren, T. Jansson, A. Eriksson, H.W. Persson, L. Kjell, Evaluation of an ultrasonic echo-tracking method for measurements of arterial wall movements in two dimensions, IEEE Trans. Ultrason. Ferroelectr. Freq. Control 52 (2005) 1300–1311.
[27] M. Larsson, F. Kremer, P. Claus, T. Kuznetsova, L.-Å. Brodin, J. D'hooge, Ultrasound-based Radial and Longitudinal Strain Estimation of the Carotid Artery: a feasibility study, IEEE Trans. Ultrason. Ferroelectr. Freq. Control 58 (2011) 2244–2251.
[28] A. Mahmoud, J. Frisbee, A. D'Audiffret, O. Mukdadi, In vivo vascular wall tissue characterization using a strain tensor measuring (STM) technique for flow-mediated vasodilation analyses, Phys. Med. Biol. 54 (2009) 6217–6238.
[29] S. Svedlund, L.M. Gan, Longitudinal common carotid artery wall motion is associated with plaque burden in man and mouse, Atherosclerosis 217 (2011) 120–124.
[30] S. Golemati, A. Sassano, M. Lever, A. Bharath, S. Dhanjil, A. Nicolaides, Carotid artery wall motion estimated from B-mode ultrasound using region tracking and block matching, Ultrasound Med. Biol. 29 (2003) 387–399.
[31] M. Larsson, F. Kremer, B. Heyde, L.-Å. Brodin, J. D'hooge, Ultrasound-based Speckle Tracking for 3D Strain estimation of the Arterial wall – An experimental validation study in a tissue mimicking phantom, in: Conference proceedings at IEEE Ultrasonics Symposium, Orlando, USA, 2011.
[32] J.T. Favreau, B.T. Nguyen, I. Gao, P. Yu, M. Tao, J. Schneiderman, G.R. Gaudette, C.K. Ozaki, Murine ultrasound imaging for circumferential strain analyses in the angiotensin II abdominal aortic aneurysm model, J. Vasc. Surg. 56 (2012) 462–469.
[33] W. Osika, F. Dangardt, J. Gronros, U. Lundstam, A. Myredal, M. Johansson, R. Volkmann, T. Gustavsson, L.M. Gan, P. Friberg, Increasing peripheral artery intima thickness from childhood to seniority, Arterioscler. Thromb. Vasc. Biol. 27 (2007) 671–676.
[34] J. Fromageau, J.L. Gennisson, C. Schmitt, R.L. Maurice, R. Mongrain, G. Cloutier, Estimation of polyvinyl alcohol cryogel mechanical properties with four ultrasound elastography methods and comparison with gold standard testings, IEEE Trans. Ultrason. Ferroelectr. Freq. Control 54 (2007) 498–509.
[35] R.G. Lopata, M.M. Nillesen, H.H. Hansen, I.H. Gerrits, J.M. Thijssen, C.L. de Korte, Performance evaluation of methods for two-dimensional displacement and strain estimation using ultrasound radio frequency data, Ultrasound Med. Biol. 35 (2009) 796–812.
[36] S. Yuda, R. Kaneko, A. Muranaka, A. Hashimoto, K. Tsuchihashi, T. Miura, N. Watanabe, K. Shimamoto, Quantitative measurement of circumferential carotid arterial strain by two-dimensional speckle tracking imaging in healthy subjects, Echocardiography 28 (2011) 899–906.
[37] A. Bjallmark, B. Lind, M. Peolsson, K. Shahgaldi, L.A. Brodin, J. Nowak, Ultrasonographic strain imaging is superior to conventional non-invasive measures of vascular stiffness in the detection of age-dependent differences in the mechanical properties of the common carotid artery, Eur. J. Echocardiogr. 11 (2010) 630–636.
[38] M. Larsson, F. Kremer, T. Kuznetsova, B. Lind, A. Bjällmark, L.-Å. Brodin, J. D'hooge, In-vivo assessment of Radial and Longitudinal Strain in the Carotid artery using Speckle tracking, IEEE International Ultrasonics Symposium, San Diego, USA, 2010.
[39] G. Zahnd, D. Vray, A. Serusclat, D. Alibay, M. Bartold, A. Brown, M. Durand, L.M. Jamieson, K. Kapellas, L.J. Maple-Brown, K. O'Dea, P. Moulin, D.S. Celermajer, M.R. Skilton, Longitudinal displacement of the carotid wall and cardiovascular risk factors: associations with aging, adiposity, blood pressure and periodontal disease independent of cross-sectional distensibility and intima-media thickness, Ultrasound Med. Biol. 38 (2012) 1705–1715.
[40] S. Svedlund, C. Eklund, P. Robertsson, M. Lomsky, L.M. Gan, Carotid artery longitudinal displacement predicts 1-year cardiovascular outcome in patients with suspected coronary artery disease, Arterioscler. Thromb. Vasc. Biol. 31 (2011) 1668–1674.